E -tunable magnetic susceptibility and reversible magnetization switching in YIG/Pt/PMN-PZT/Pt heterostructure by low electric and magnetic fields

Liuyang Han, Freddy Ponchel, Denis Remiens, Tuami Lasri, Nicolas Tiercelin, Genshui Wang, Philippe Pernod

E-tunable magnetic susceptibility and reversible magnetization switching in YIG/Pt/PMN-PZT/Pt heterostructure by low electric and magnetic fields

Liuyang Han[1,2], Freddy Ponchel[1], Denis Rémiens[1], Tuami Lasri[1], Nicolas Tiercelin[1], Genshui Wang[2,3], *and* Philippe Pernod[1]

[1]Univ. Polytechnique Hauts-de-France, CNRS, Centrale Lille, ISEN, Univ. Lille, UMR 8520-IEMN, Joint International Laboratory LIA LICS/LEMAC, Lille 59000, France
[2]Key Laboratory of Inorganic Functional Materials and Devices and State Key Laboratory of High Performance Ceramics and Superfine Microstructure, Shanghai Institute of Ceramics, Chinese Academy of Sciences, Shanghai 200050, People's Republic of China
[3]Center of Materials Science and Optoelectronics Engineering, University of Chinese Academy of Sciences, Beijing 100049, China

Abstract

The electric field (E) controlled magnetism in the multiferroic heterostructure comprising polycrystalline yttrium iron garnet (YIG) film, Pt electrodes, and lead magnesium niobate-lead zirconate titanate (PMN-PZT) ceramic is presented in this work. The electric-field-dependent magnetization and susceptibility of YIG film reveal the strain-mediated transformation of magnetocrystalline anisotropy. A strong converse magnetoelectric (CME) effect has been observed in the YIG/Pt/PMN-PZT/Pt heterostructure, and the CME coefficient can reach 17×10^{-8} s/m at 0 Oe and 4.2 kV/cm. The reversible magnetization switching by means of a low voltage pulse (±4.6 kV/cm) can be realized at 0 Oe in the YIG/Pt/PMN-PZT/Pt heterostructure, and the E-tunable susceptibility can reach $\Delta\chi/\chi_{0+} = 55.5\%$ at 20 Oe and 4 kV/cm. These results show great potential in power-efficient magnetoelectric components for information storage and tunable devices.

1. Introduction

Multiferroic materials with two or more ferroic properties (ferroelectricity, ferromagnetism, ferroelasticity, etc.) have been largely studied in the last several years, and exciting progress has been made recently in novel multiferroic materials and devices.[1–4] The magnetoelectric (ME) materials, which display ferroelectricity and ferromagnetism simultaneously, can be obtained from single-phase multiferroic compounds or artificial composites. The "artificial" ME composites have been largely demonstrated, and various couples of different ferroelectric (FE) and ferromagnetic (FM) materials lead to many different applications, such as magnetic sensors, magnetoelectric random access memories, and voltage tunable microwave devices such as phase shifters, resonators, filters, etc.[5–12]

Magnetoelectric coupling in composites or heterostructures can be mediated by the strain transfer between the FE and FM phases. For the converse magnetoelectric coupling effect (CME), the electric field (E) induced strain generated in FE materials is transferred to FM materials and leads to the change of magnetism. The FE materials used for CME coupling are usually materials with large E-induced strain, such as Pb(Zr, Ti)O_3 ceramics and $Pb(Mg_{1/3}Nb_{2/3})O_3$-$PbTiO_3$ single crystals.[9,12–14] The $0.25Pb(Mg_{1/3}Nb_{2/3})O_3$-$0.75Pb(Zr_{0.48}Ti_{0.52})O_3$ (PMN-PZT) ceramic is chosen as the piezoelectric phase in this work due to its high E-induced strain and its excellent electrical properties. The composition of 0.25PMN-0.75PZT is around the morphotropic phase boundary, where excellent piezoelectric performance exists.[15] The coercive field (E_C) of PMN-PZT ceramics is as low as 4.2 kV/cm, while the E-induced strain can reach 0.28% at E_C.

Ferrite yttrium iron garnet (YIG) has attracted much attention over the years because of its predominant advantages for microwave devices. YIG properties such as low losses, narrow ferromagnetic resonance (FMR) linewidth, and a wide range of magnetic tunability are essential

assets for microwave device technology. Thus, much work has been devoted to YIG/FE multiferroic heterostructure, especially in voltage tuning of FMR.[9,12,13,16] In fact, the *E*-controlled FMR shift is an indirect method to characterize the CME coupling effect according to the definition of the CME coefficient. However, the most direct manifestation of the CME effect, the *E*-controlled magnetization variations of YIG/FE, is less studied. Lian *et al.* were first to demonstrate the *E*-controlled magnetization in the composite of thickness-dependent YIG film on PMN-PZT ceramics,[17,18] and a good CME effect has been achieved. Potential applications can be developed, such as in voltage writing of magnetic bits.[4,19,20] These magnetoelectric components show significant advantages in improving the efficiency of power electronics.[21] It is interesting to note that previous researchers have worked on various systems to achieve the giant CME coupling effect with an absence of external magnetic field in resonance frequency[22–26] and the *E*-controlled remnant magnetization variations.[27–29] The absence of an external magnetic field can eliminate the use of the DC magnetic bias field and provides great potential for miniaturized and integrated device applications. In this paper, we report on the work on *E*-controlled magnetization switching and *E*-tunable susceptibility with an applied electric field whose magnitude is close to E_C; these properties have not been reported in YIG/PMN-PZT composite yet.

In particular, we have demonstrated that, with a multiferroic heterostructure constituted by a ferrite YIG film deposited on a PMN-PZT ceramic, a low-voltage-pulse induced reversible magnetization switching of YIG/Pt/PMN-PZT/Pt heterostructures is realized at 0 Oe, and a large *E*-tunable susceptibility with a low magnetic field is achieved. The results demonstrate great potential for power-efficient *E*-controlled nonvolatile memories and magnetoelectric tunable devices.

2. Experiments

Figure 1(a) schematically illustrates the multiferroic heterostructure of YIG/PMN-PZT. The insulated YIG film and PMN-PZT ceramic are combined with Pt electrodes as the interlayer. The PMN-PZT ceramic was prepared by a conventional solid-state reaction and was well-polished.[15] The Pt electrodes whose thickness is 80 nm were deposited by DC magnetron sputtering on both sides of the PMN-PZT ceramic. Then, the 400 nm thick YIG film was deposited on one side of the Pt/PMN-PZT/Pt structure by radio frequency magnetron sputtering. The sputtering conditions and postannealing process is given in Ref. 18. The thickness of 400 nm was selected according to a previous study that demonstrated the influence of the YIG film thickness on the CME coupling.[17] The dimensions of the ceramic substrate are designed to be $8 \times 8\ \text{mm}^2$, while Pt electrodes and YIG film size are restricted to be $6 \times 6\ \text{mm}^2$ and $5 \times 3\ \text{mm}^2$ by masks, respectively. In order to apply the electric field, a soldering process was involved in connecting conductive wires with Pt electrodes. Thus, the magnetic field and electric field can be applied to the sample simultaneously, and the direction of the fields is indicated on the figure. The electric hysteresis loop (*P*-*E*) and field-induced strain curve (*S*-*E*) of the PMN-PZT were measured at a frequency of 1 Hz with a standard ferroelectric tester (TF analyzer 2000, aixACCT, Germany), as shown in Fig. 1(b). The butterfly *S*-*E* curve of PMN-PZT shows a very sharp strain peak at the coercive electric field. One can note that the strain level rises from –0.28% at 4.2 kV/cm to +0.12% at 12 kV/cm.

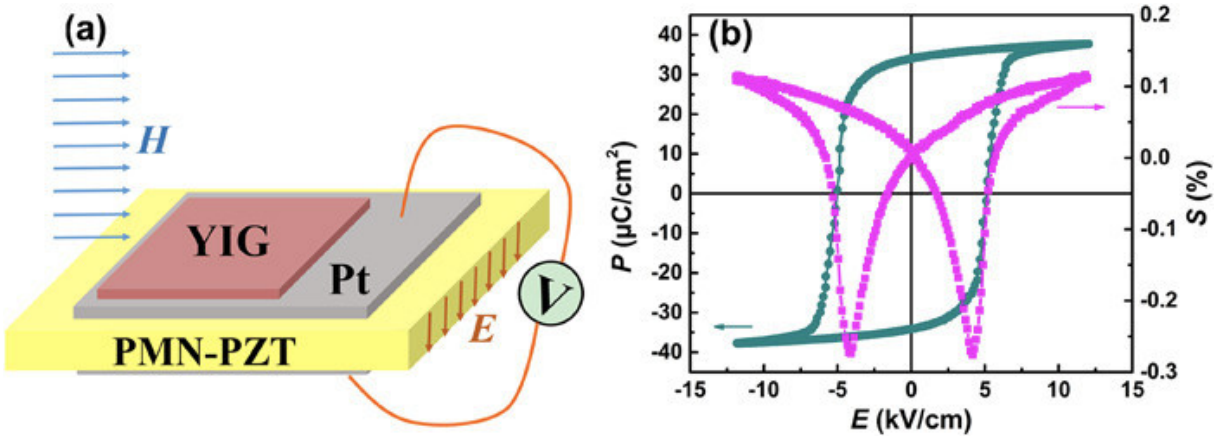

FIG. 1. (a) Schematic of the YIG/Pt/PMN-PZT/Pt magnetoelectric heterostructure, and (b) (*P*-*E*) loop and (*S*-*E*) curve of the PMN-PZT ceramic

The phase structure and crystallization of the YIG/Pt/PMN-PZT/Pt laminate composite were analyzed by X-ray diffraction (XRD, D/MAX-2550 V; Rigaku, Tokyo, Japan). The XRD analysis confirms the expected phase structures for all the materials. The origin of the various peaks is as labeled in Fig. 2(a). Even though the diffraction peaks of YIG thin films are of much lower intensity when compared to the peaks of PMN-PZT ceramic and Pt electrodes, they are distinct enough, and all correspond to the pure YIG phase. Then, cross-sectional morphology was characterized by a scanning electron microscope (SEM, S4800; Hitachi, Tokyo, Japan), as shown in Fig. 2(b). The clear interface between the different materials, PMN-PZT ceramic, Pt electrode, and YIG film, indicates that no discernable diffusion happened.

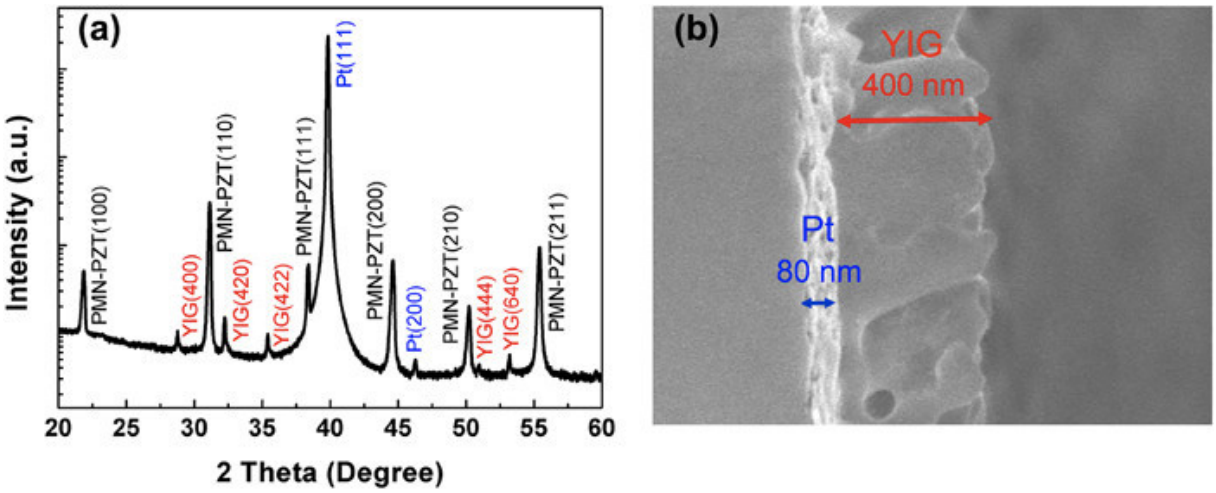

FIG. 2. (a) The XRD pattern and (b) cross-sectional SEM image of the YIG/Pt/PMN-PZT/Pt heterostructure.

Finally, the magnetic hysteresis loops (*M*-*H*) with different electric fields and the electric field tuning of magnetization (*M*-*E*) were measured at room temperature by a Vibration Sample Magnetometer (VSM, ADE model EV9) combined with an external DC voltage supply. The external magnetic field and electric field can be applied to the sample at the same time to obtain *M*-*H* and *M*-*E* curves. Before the measurements of magnetic properties, it is necessary to calibrate the measurements to offset the influence of the substrate, electrodes, and wires. To that end, a reference sample is used (Pt/PMN-PZT/Pt). Thanks to this calibration process, only the magnetic response of the YIG film is recorded.

3. Results and discussion

The electric field dependence of magnetic hysteresis (*M*-*H*) loops of the YIG/Pt/PMN-PZT/Pt heterostructure is illustrated in Fig. 3(a). First, it is noticed that without the application of an

electric field, the YIG film shows good magnetic properties on PMN-PZT ceramic substrate and the coercive magnetic field (H_C) and the remnant magnetization (M_r) are found to be equal to 24.5 Oe and about 30 emu/cm^3, respectively. Then, one can observe that when an electric field is applied, the shape of (M-H) loops varies with the electric-field-induced strain. Since the PMN-PZT reaches the maximum negative strain at $E = E_C$ and the maximum positive strain at $E = E_{max}$, the (M-H) loops of YIG/Pt/PMN-PZT/Pt at electric fields of −4 kV/cm and 12 kV/cm are given as representatives. It can be seen that the positive strain tends to upright (M-H) loops, while the negative strain tends to slanted (M-H) loops, revealing the strain-mediated transformation of magnetocrystalline anisotropy. It also reveals that the distinct E-induced magnetization variations occur at low magnetic fields [as zoomed in the inset (0–300 Oe)], while the E-induced magnetization variations are small at the saturated magnetic field. In Fig. 3(b), the remnant magnetization (M_r) and coercive magnetic field (H_C) variation as a function of the electric field are given. The large strain change at $E = E_C$ results in a large jump in magnetization at an electric field of −4 kV/cm, and the H_C shifts up to 28.8 Oe. Additionally, it is exhibited that the (M_r-E) and (H_C-E) curves of the YIG/Pt/PMN-PZT/Pt heterostructure present a similar butterfly shape to the (S-E) curve of the PMN-PZT ceramic, which is attributed to the strain-mediated coupling effect.

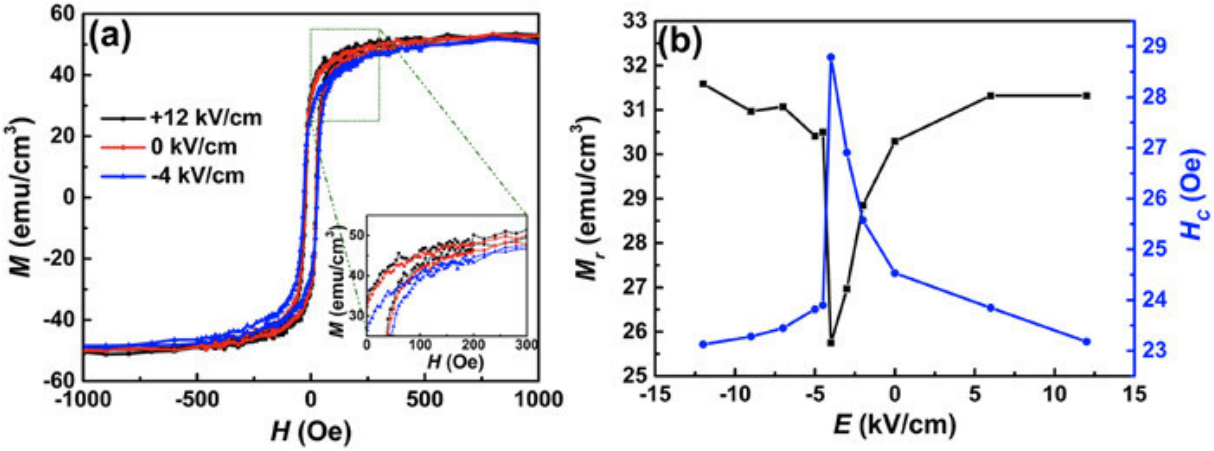

FIG. 3. (a) (M-H) loops with different electric fields; inset: the enlarged (M-H) loops; (b) (M_r-E) and (H_C-E) curves of the YIG/Pt/PMN-PZT/Pt heterostructure.

The slope variations of (M-H) loops under different electric fields refer to the shift in magnetic susceptibility (χ) manipulated by the electric field. Figure 4 presents the (χ-H) curves for three electric fields and the (χ-E) curve for different magnetic fields (5, 10, 15, 20, and 25 Oe) in YIG/Pt/PMN-PZT/Pt heterostructure. Under a specific electric field, the χ reaches its peak value at H_C. The value of H_C varies with different electric fields. Thus, the χ peaks at different magnetic fields (20–30 Oe) under different electric fields. In a magnetic field range from 5 to 25 Oe, the χ variations under different electric fields are quite apparent from Fig. 4(a). Thus, the E-controlled χ variations for magnetic fields of 5, 10, 15, 20, and 25 Oe are given in Fig. 4(b). If we consider the results obtained at 20 Oe, it can be seen that the χ changes dramatically with an external electric field, being 33.6 at 12 kV/cm, 27.6 at the zero field, and 15.5 at E_C. This equals a large tunable susceptibility of $\Delta\chi = 18.1$ and a relative variation of $\Delta\chi/\chi_0 = 65.6\%$ (χ_0 is the value at zero field). These values obtained under a low magnetic field of 20 Oe suggest great potential in ME tunable devices. The tunable susceptibility relative variation $\Delta\chi/\chi_0$ calculated for magnetic fields of 15 Oe and 25 Oe is 80.4% and 28.5%, respectively.

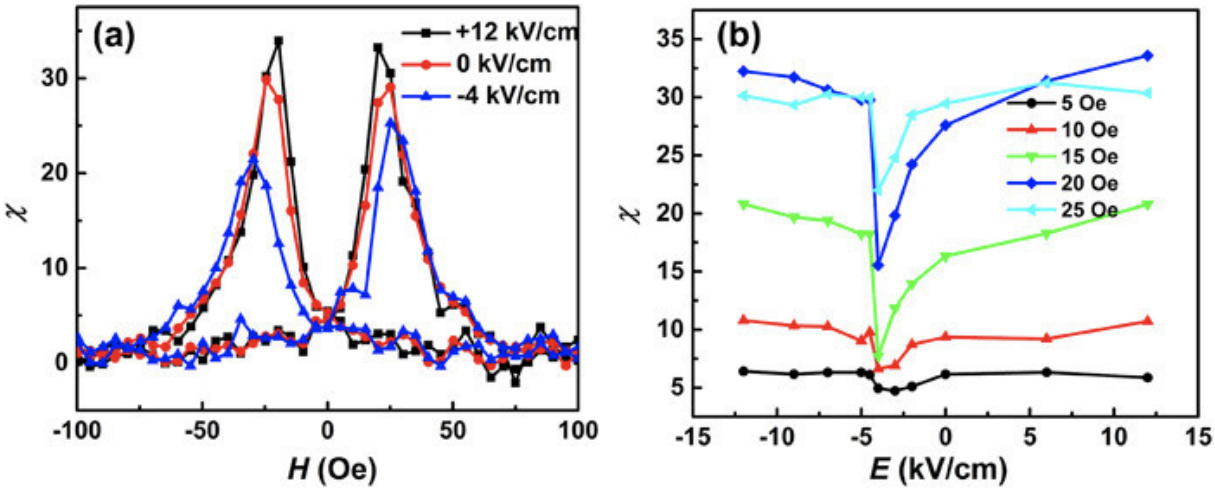

FIG. 4. (a) (χ-H) curves for different electric fields and (b) (χ-E) curves at 5, 10, 15, 20, and 25 Oe of the YIG/Pt/PMN-PZT/Pt heterostructure.

The relative magnetization change ($\Delta M/M_0$) of the YIG/Pt/PMN-PZT/Pt heterostructure is given in Fig. 5(a) as a function of the electric field at 0 Oe. The butterflylike shape of the ($\Delta M/M_0$-E) curve resembles the S-E curve observed in the PMN-PZT ceramic, which once again confirms that the change in magnetization in the YIG film results from the E-induced strain in the PMN-PZT ceramic. The positive strain favors the magnetization process, while the negative strain leads to a demagnetization process. The large negative strain at E_C facilitates a sharp reduction in magnetization, which yields a maximum of ($\Delta M/M_0$) variations. As a consequence, the CME coefficient [$\alpha_{CME} = \mu_0 \delta M/\delta E$ ($\mu_0 = 4\pi \times 10^{-7}$ H/m)] peaks at E_C, reaching a large value of 17×10^{-8} s/m (α_{CME} in the absence of a bias magnetic field), as shown in Fig. 5(b). Therefore, these results demonstrate the possibility to achieve a strong ME effect under a small electric field and zero magnetic field, which promotes the realization of power-efficient ME devices.

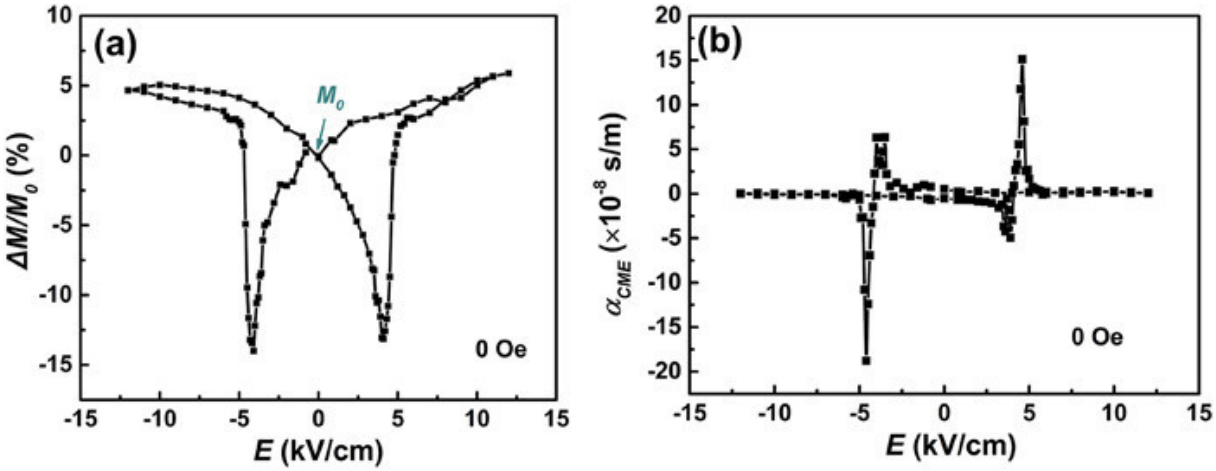

FIG. 5. (a) ($\Delta M/M_0$-E) and (b) (α_{CME}-E) curves at 0 Oe of the YIG/Pt/PMN-PZT/Pt heterostructure.

The α_{CME} as a function of the bias magnetic field is presented in Fig. 6. One can note that the α_{CME} firstly rises and then decreases with the bias magnetic field. The maximum of α_{CME} (18×10^{-8} s/m) appears at 25 Oe, which can be attributed to the ease of switching the magnetization at this point because the H_C is close to this value. When the bias magnetic field is higher than H_C, the electric-field-induced demagnetization process is hindered by a large bias magnetic field that results in a low CME coefficient.

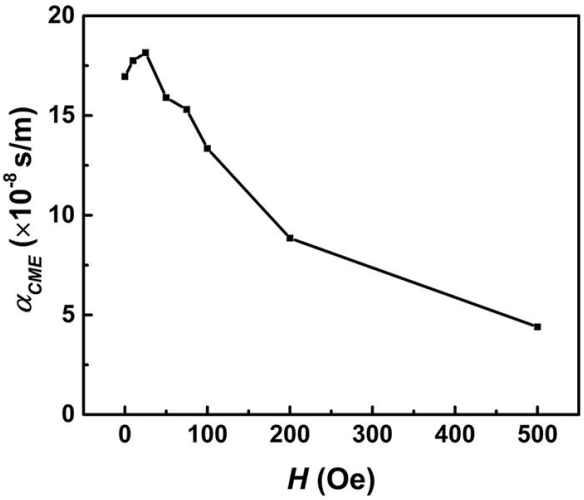

FIG. 6. The (α_{max}-H) curves of the YIG/Pt/PMN-PZT/Pt heterostructure.

Since the E-induced strain plays a crucial role in the ME coupling effect, the (S-E) curves of the PMN-PZT ceramic measured by a cycling electric field with different amplitudes are depicted in Fig. 7(a). When the amplitude of E is much higher than E_C, a whole butterflylike curve appeared because of the complete ferroelectric domain switching. While for $E \leq E_C$, a shuttle-like curve was observed due to incomplete ferroelectric domain switching, which results in large remnant strain. Thus, two different strain states are generated when $E \leq E_C$, leading to two magnetization states in the YIG film. Figure 7(b) demonstrates the magnetization curves under different electric field amplitude cycling at 0 Oe, which is consistent with the observed (S-E) curves. The inclined direction of asymmetric (M-E) curves depends on the electric field history. When $E \leq E_C$, the two magnetization states can be reached through the strain-mediated CME coupling effect.

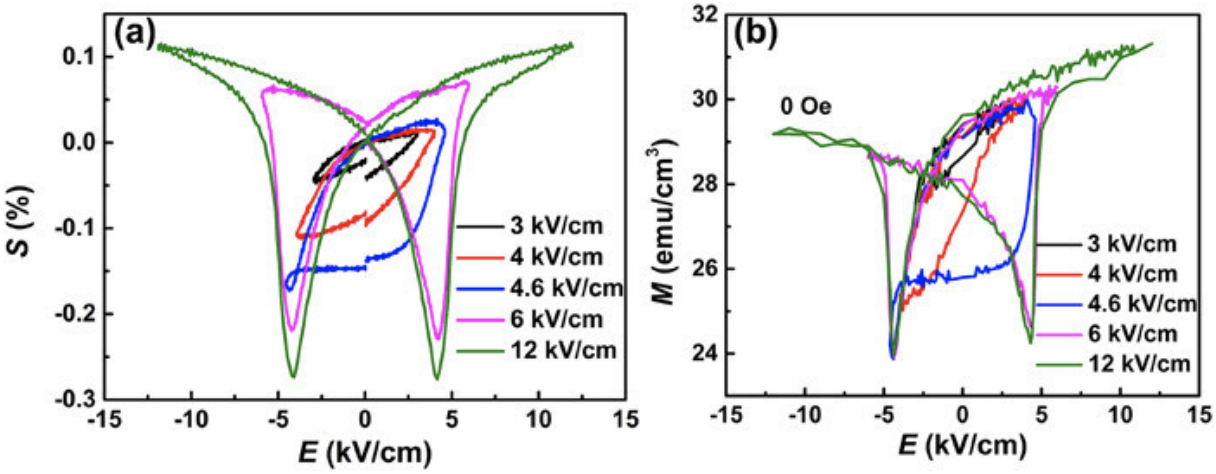

FIG. 7. (a)The (S-E) curves and (b) (M-E) curves of the YIG/Pt/PMN-PZT/Pt heterostructure by a cycling electric field with different amplitudes.

The results of Fig. 7 confirm the potential of the YIG/Pt/PMN-PZT/Pt heterostructure with low amplitudes of cycling electric field for magnetoelectric memory devices and tunable device applications. Indeed, the two E-controlled distinct remnant magnetization states (E amplitude equal to 4.6 kV/cm) allow applications in energy-efficient ME random access memory devices. In addition, when the amplitude of E equals 4 kV/cm, the slim shuttlelike M-E curve indicates high and linear E-tunable susceptibility for RF/microwave magnetic devices.

In order to simulate a real memory writing process, a dynamic voltage pulse induced of 4.6 kV/cm and −4.6 kV/cm is applied alternately at a period of 60 s, as given in Fig. 8. As an E-field pulse of 4.6 kV/cm is applied, the magnetization in the YIG film rises and then remains at a magnetization ratio of 54.4%, which means a switch from the state “1” to state “0”.

Similarly, the magnetization is reduced and then stayed at a magnetization ratio of 48.2% when an E-field pulse of −4.6 kV/cm is applied, indicating the switching from "0" to "1". Therefore, dynamic *E*-field-pulse-induced magnetization switching in the YIG film is realized with a zero magnetic field and a low electric field of 4.6 kV/cm. This type of memory by switching the magnetization would result in nonvolatile magnetization tuning with low power consumption.

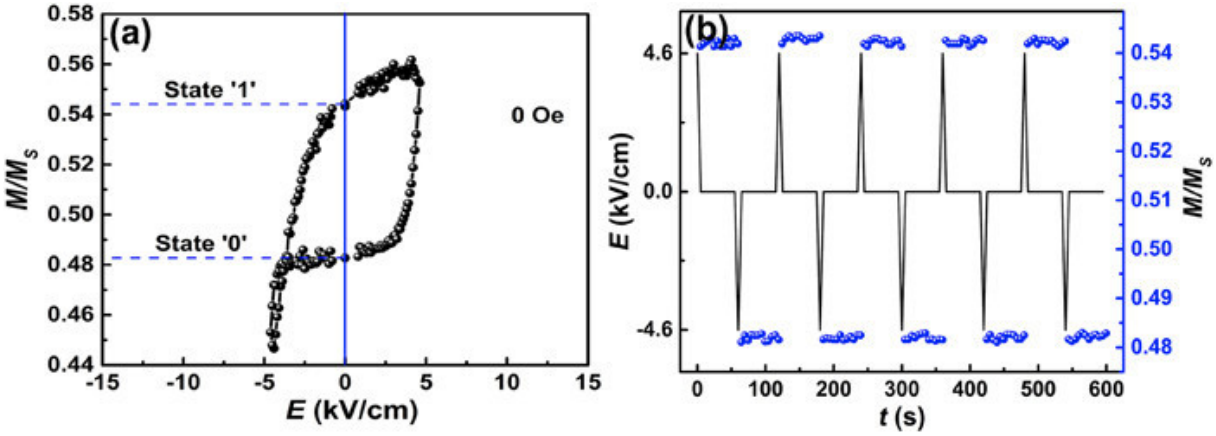

FIG. 8. (a) The *M*-*E* curve with an electric field cycle from −4.6 kV/cm to 4.6 kV/cm; (b) the time-dependent magnetization switched by the electric field at 0 Oe of the YIG/Pt/PMN-PZT/Pt heterostructure.

The *E*-tunable susceptibility variations of YIG/Pt/PMN-PZT/Pt heterostructure are presented in Fig. 9. By applying a cycle of the electric field with an amplitude of 4 kV/cm, the linearlike slanted (χ-*E*) curve is observed, and the χ varies in the range from 15.5 to 32.9 at 20 Oe. The large *E*-tunable susceptibility ratio can reach $\Delta\chi/\chi_{0+} = 55.5\%$ at 20 Oe with a cycling electric field of 4 kV/cm, which indicates a promising way to fabricate *E*-tunable inductors.[30] Other than conventional magnetic components or devices, where tunability is achieved by adjusting the magnetic field, *E*-tunable magnetic devices offer more substantial flexibility and lower energy consumption.[31]

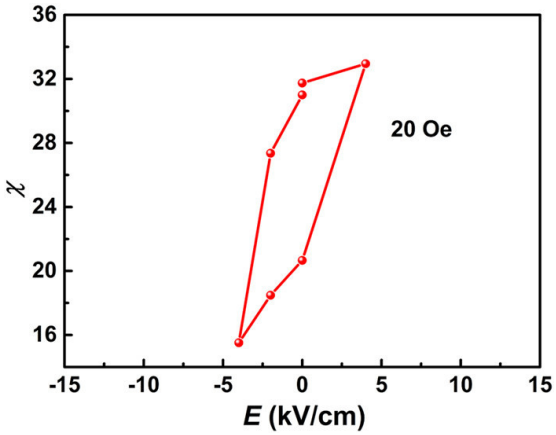

FIG. 9. The (χ-*E*) curve with an electric field cycle from −4 kV/cm to 4 kV/cm at 20 Oe of the YIG/Pt/PMN-PZT/Pt heterostructure.

4. Conclusions

In conclusion, we have carefully investigated the *E*-controlled magnetism in the YIG/Pt/PMN-PZT/Pt heterostructure. The electric-field-dependent (*M*-*H*) loops and (χ-*H*) curves reveal the strain-mediated transformation of magnetocrystalline anisotropy in the YIG film. As a result, the *E*-controlled *Mr*, H_C, and χ change correspondingly with the PMN-PZT ceramic's strain evolution. The CME coefficient can reach 17×10^{-8} s/m in the absence of a bias magnetic field at the E_C of the PMN-PZT ceramic, and the maximum CME coefficient (18×10^{-8} s/m) is observed under the magnetic and electric fields of 25 Oe and 4.2 kV/cm, respectively,

demonstrating a strong converse magnetoelectric coupling effect in the YIG/Pt/PMN-PZT/Pt heterostructure. When the electric field amplitude applied is close to the E_C of PMN-PZT, the *E*-induced shuttle-like strain evolution of PMN-PZT favors two possible applications in the YIG/Pt/PMN-PZT/Pt heterostructure. On the one hand, two distinct remnant strain states lead to two stable magnetization states of the YIG film. The voltage-pulse reversible magnetization switching of YIG/Pt/PMN-PZT/Pt heterostructures is realized at 0 Oe with an electric field pulse of ±4.6 kV/cm, which shows the feasibility of power-efficient *E*-controlled nonvolatile memories. On the other hand, the linear *E*-tunable susceptibility change can be realized at 20 Oe and 4 kV/cm, and the tunable susceptibility can reach $\Delta\chi/\chi_{0+} = 55.5\%$, indicating the potential for power-efficient magnetoelectric tunable devices.

Acknowledgements

This work is financially supported by the Ph.D. contract of Université Polytechnique Hauts-de-France, the International Partnership Program of Chinese Academy of Sciences (Grant No. GJHZ1821), and the Chinese Academy of Sciences President's International Fellowship Initiative (Grant No. 2017VEA0002).

References

1. W. Eerenstein, N. D. Mathur, and J. F. Scott, Nature **442**, 759 (2006
2. Y. Wang, J. Hu, Y. Lin, and C.-W. Nan, NPG Asia Mater. **2**, 61 (2010)
3. C.-W. Nan, M. I. Bichurin, S. Dong, D. Viehland, and G. Srinivasan, J. Appl. Phys. **103**, 031101 (2008).
4. J.-M. Hu, T. Nan, N. X. Sun, and L.-Q. Chen, MRS Bull. **40**, 728 (2015).
5. G. Srinivasan, Annu. Rev. Mater. Res. **40**, 153 (2010)
6. J. Zhai, Z. Xing, S. Dong, J. Li, and D. Viehland, J. Am. Ceram. Soc. **91**, 351 (2008).
7. T. X. Nan, Z. Y. Zhou, J. Lou, M. Liu, X. Yang, Y. Gao, S. Rand, and N. X. Sun, Appl. Phys. Lett. **100**, 132409 (2012)
8. A. S. Tatarenko, G. Srinivasan, and M. I. Bichurin, Appl. Phys. Lett. **88**, 183507 (2006).
9. X. Yang, Y. Gao, J. Wu, Z. Zhou, S. Beguhn, T. Nan, and N. X. Sun, IEEE Microw. Wirel. Compon. Lett. **24**, 191 (2014).
10. A. B. Ustinov, G. Srinivasan, and Y. K. Fetisov, J. Appl. Phys. **103**, 063901 (2008).
11. Y. K. Fetisov and G. Srinivasan, Appl. Phys. Lett. **88**, 143503 (2006).
12. A. S. Tatarenko, V. Gheevarughese, G. Srinivasan, O. V. Antonenkov, and M. I. Bichurin, J. Electroceram. **24**, 5 (2010).
13. C. Pettiford, S. Dasgupta, J. Lou, S. D. Yoon, and N. X. Sun, IEEE Trans. Magn. **43**, 3343 (2007).
14. C. Thiele, K. Dörr, O. Bilani, J. Rödel, and L. Schultz, Phys. Rev. B **75**, 054408 (2007).
15. L. Wang, R. Liang, C. Mao, G. Du, G. Wang, and X. Dong, Ceram. Int. **39**, 8571 (2013).
16. A. B. Ustinov, Y. K. Fetisov, and G. Srinivasan, Tech. Phys. Lett. **34**, 593 (2008).
17. J. Lian, F. Ponchel, N. Tiercelin, Y. Chen, D. Rémiens, T. Lasri, G. Wang, P. Pernod, W. Zhang, and X. Dong, Appl. Phys. Lett. **112**, 162904 (2018)
18. J. Lian, F. Ponchel, N. Tiercelin, L. Han, Y. Chen, D. Rémiens, T. Lasri, G. Wang, P. Pernod, W. Zhang, and X. Dong, J. Appl. Phys. **124**, 064101 (2018)
19. A. Klimov, N. Tiercelin, Y. Dusch, S. Giordano, T. Mathurin, P. Pernod, V. Preobrazhensky, A. Churbanov, and S. Nikitov, Appl. Phys. Lett. **110**, 222401 (2017).
20. S. Lepadatu, M. Vopson, S. Lepadatu, and M. M. Vopson, Materials **10**, 991 (2017).
21. M. M. Vopson, Crit. Rev. Solid State Mater. Sci. **40**, 223 (2015)
22. S. Chul Yang, K.-H. Cho, C.-S. Park, and S. Priya, Appl. Phys. Lett. **99**, 202904 (2011).
23. J. Zhang, P. Li, Y. Wen, W. He, A. Yang, D. Wang, C. Yang, and C. Lu, Appl. Phys. Lett. **105**, 172408 (2014).
24. J. Zhang, P. Li, Y. Wen, W. He, A. Yang, C. Lu, and C. Yang, IEEE Trans. Magn. **50**, 1000104 (2014).

25. Z. Zuo, Q. Zhan, G. Dai, B. Chen, X. Zhang, H. Yang, Y. Liu, and R.-W. Li, J. Appl. Phys. **113**, 17C705 (2013).
26. C. Yang, P. Li, Y. Wen, A. Yang, D. Wang, F. Zhang, and J. Zhang, IEEE Trans. Magn. **51**, 1000404 (2015).
27. M. Liu, O. Obi, J. Lou, S. Stoute, J. Y. Huang, Z. Cai, K. S. Ziemer, and N. X. Sun, Appl. Phys. Lett. **92**, 152504 (2008).
28. M. Liu, O. Obi, J. Lou, Y. Chen, Z. Cai, S. Stoute, M. Espanol, M. Lew, X. Situ, K. S. Ziemer, V. G. Harris, and N. X. Sun, Adv. Funct. Mater. **19**, 1826 (2009)
29. M. Liu, J. Lou, S. Li, and N. X. Sun, Adv. Funct. Mater. **21**, 2593 (2011).
30. Y. Yan, L. D. Geng, L. Zhang, X. Gao, S. Gollapudi, H.-C. Song, S. Dong, M. Sanghadasa, K. Ngo, Y. U. Wang, and S. Priya, Sci. Rep. **7**, 16008 (2017)
31. M. Liu, Z. Zhou, T. Nan, B. M. Howe, G. J. Brown, and N. X. Sun, Adv. Mater. **25**, 1435 (2013).